Solution-based synthesis of cobalt-doped ZnO thin films

Published in:
Thin Solid Films

Document Version:
Peer reviewed version

Queen's University Belfast - Research Portal:
Link to publication record in Queen's University Belfast Research Portal

Accepted Manuscript

Solution-based synthesis of cobalt-doped ZnO thin films

Sesha Vempati, Amitha Shetty, P. Dawson, K.K. Nanda, S.B. Krupanidhi

Please cite this article as: Sesha Vempati, Amitha Shetty, P. Dawson, K.K. Nanda, S.B. Krupanidhi, Solution-based synthesis of cobalt-doped ZnO thin films, *Thin Solid Films* (2012), doi: 10.1016/j.tsf.2012.10.008

Solution-based synthesis of cobalt-doped ZnO thin films

Sesha Vempati

School of Mathematics and Physics, Queen's University Belfast, BT7 1NN, UK,

Amitha Shetty

Materials Research Center, Indian Institute of Science, Bangalore – 560012, India.

P. Dawson*

School of Mathematics and Physics, Queen's University Belfast, BT7 1NN, UK,

K. K. Nanda and S.B. Krupanidhi

Materials Research Center, Indian Institute of Science, Bangalore – 560012, India.

Corresponding author: p.dawson@qub.ac.uk

Abstract

Undoped and cobalt-doped (1-4 wt%) ZnO polycrystalline, thin films have been fabricated on quartz substrates using sequential spin-casting and annealing of simple salt solutions. X-ray diffraction (XRD) reveals a wurzite ZnO crystalline structure with high-resolution transmission electron microscopy showing lattice planes of separation 0.26 nm, characteristic of (002) planes. The Co appears to be tetrahedrally co-ordinated in the lattice on the Zn sites (XRD) and has a charge of +2 in a high-spin electronic state (X-ray photoelectron spectroscopy). Co-doping does not alter the wurzite structure and there is no evidence of the precipitation of cobalt oxide phases within the limits of detection of Raman and XRD analysis. Lattice defects and chemisorbed oxygen are probed using photoluminescence and Raman spectroscopy – crucially, however, this transparent semiconductor material retains a bandgap in the ultraviolet (3.30 - 3.48 eV) and high transparency (throughout the visible spectral regime) across the doping range.

Keywords: ZnO; transparent semiconductor; optical materials

1. Introduction

Controlled synthesis of ZnO nanostructures and thin films and an in-depth understanding of their chemical/physical properties and electronic structure are key to the development of ZnO-based (nano) devices. In particular, in this article we address the synthesis and properties of Co-doped ZnO as an interesting class of transparent semiconductor with, also, potential functionality as a dilute magnetic semiconductor at room temperature. Although it is acknowledged that the origin of ferromagnetism in transition-metal doped ZnO is not yet very well understood [1] it is nonetheless clear that ZnO is a candidate material for room temperature semiconductor (bipolar) spintronics, as evidenced by increasing interest in experimental studies of in this area [2-5]. However, optical and electrical properties also play a major role in determining the importance and utility of doped ZnO. The increased functionalities in dilute ferromagnetic semiconductors via spin-polarized electron transport opens up various potential applications [6-8]. Moreover, if an optically transparent ferromagnetic dilute magnetic semiconductor can be made, then it would be attractive for optospintronic applications [9, 10]. In this regard also ZnO is a suitable host material as it possesses a large band gap and large excitonic binding energy that lie in the ultraviolet region of the spectrum.

ZnO has been synthesized in a variety of ways, including pulsed laser deposition [11], chemical vapor transport [12], electrodeposition [13], co-precipitation [14] and solid state reaction [15]. While simpler synthesis techniques that can be performed in ambient environment have the attraction of wider accessibility and low-cost it is, of course, very important that the (doped) ZnO thus produced is of high integrity, displaying comparable properties and competitive functionality with that produced by other means. A popular route in low-cost materials fabrication is sol-gel processing where hydrates of the various constituents need to be

prepared; this method has been employed to prepare thin films of Co-doped ZnO [16]. In the work reported here, however, we have adopted an even more direct methodology based on decomposition of metal salts via oxidation at high temperature. The form of the resulting ZnO material is generally highly structured on the micro- to nano-scale. In this work the solution-based methodology leads to a uniform polycrystalline thin film that can serve as a basis for subsequent structuring and device fabrication.

2. Experimental details

Zinc nitrate and cobalt chloride (both Sigma Aldrich) were used as received with the required amounts of these salts being dissolved in ethanol. The solutions were spincast at ~800 r.p.m. on a quartz slide which was then placed in a furnace at 600 °C for 6 h. Repeating this process 10-15 times yields uniform films of thickness nearly 25 nm. We have investigated four concentrations of Co doping 1, 2, 3, 4 wt% along with pristine ZnO. For convenience we refer to these samples as ZC1, ZC2, ZC3, ZC4, and ZnO. Surface morphological studies were performed via tapping mode, atomic force microscopy (AFM) using a Digital Instruments, Nanoscope IIIa. Field emission transmission electron microscopy (FETEM, operating at 200 kV) measurements were made with a Philips Tecnai F20 FETEM and X-ray diffraction (XRD) analysis was carried out with a Bruker-AXS D8 4-circle thin film X-ray diffractometer (CuKα = 1.5418 Å) in standard θ-2θ, Bragg-Brentano configuration. X-ray photoelectron spectroscopy (XPS) measurements were performed at a pressure in the low 10^{-6} mbar range using a Thermoscientific Multilab 2000, employing the AlKα line at 1486.6 eV. The binding energy scale was referenced to the silver spectrum originating from the silver epoxy used to secure the sample. The peak fitting was carried out with Origin 6.1 software where semi-automated background subtraction was utilised. All the peaks were fitted with a single Gaussian curve except those displaying an

observable asymmetry – the exceptions were the peaks for the O1s line where a de-convolution into two or three Gaussian peaks was performed (see section 3.2.3). No constraints were used in the fitting of single peaks, while only the number of peaks was constrained in the multiple peak fits, according to the goodness of fit achieved. Optical investigations constituted photoluminescence (PL) measurements using a pulsed excitation laser at 355 nm (MPL-355 from CNI) and Andor SR163 spectrometer with CCD camera, optical absorption studies using a Perkin-Elmer Lambda 850 spectrophotometer and Raman spectroscopy using a lab-built system with an input laser at 532 nm (also CNI).

3. Results

3.1 Morphology

AFM images are shown in Fig. 1 for ZC1-4 and these serve to illustrate that the deposited films are indeed continuous and of polycrystalline nature. It is noticeable that the more heavily doped samples, ZC3 and ZC4, actually possess the better-developed grain structure, with grain sizes on the order of 100-150 nm. This gives an initial indication that, on the local (crystallite) scale at least, these samples may possess the better crystalline structure, possibly with fewer defects and associated defect signatures. This tentative observation is, in fact, markedly confirmed in the Raman spectroscopy data presented below. The variation of grain size from sample to sample, and indeed within samples, is likely due to non-uniformity in the evaporation process at each spin-casting stage in the film formation. The film morphology itself can be an important feature influencing, for example, the fill factor of photovoltaic devices and, in turn, the overall device performance. [17]

3.2 Crystal structure and electronic configuration of the constituent atoms

3.2.1 TEM analysis

High resolution TEM (HRTEM) and selected area electron diffraction (SAED) data are shown in Fig. 2 for ZC1 and ZC3. In the HRTEM images well-defined boundaries of planes in different orientations are observed. The SAED patterns indicate a qualitative difference between the samples where that for ZC3 shows well-defined diffraction spots characteristic of a single, well-defined small crystallite. On the other hand the pattern from ZC1 is rather diffuse, but with polycrystalline-type ring structure where the diffracting planes are identified in the SAED patterns of Fig. 2. The stronger circles correspond to diffraction from the (100) and (101) planes which are also strongly evident in the XRD diffractograms of Fig. 3 for this sample (section 3.2.2). The better crystalline quality of ZC3 is underscored in the HRTEM image where the diffracting planes are parallel over the image (in contrast to ZC1) and the interplanar spacing is practically constant at the expected value of 0.26 nm for (002) planes. The SAED pattern for ZC3 might reasonably be expected from a single, larger crystalline grain as noted in the AFM image of Fig. 2 while the diffuse SAED pattern yielded by ZC1 is qualitatively consistent with the much smaller, less well -organized grains shown in the corresponding AFM image.

Finally, it is noted in the context of the electron microscopy analysis that estimates of the Co concentration using EDX analysis (not shown here) shows that the actual concentration of Co is 1.06, 2.05, 3.14 and 4.15% (within a maximum error range of ±10%) for the nominal 1% to 4% dopant levels used for sample identification here.

3.2.2 XRD analysis

The diffraction patterns from ZnO through ZC1-4 are shown in Fig. 3, with the observed peaks corresponding to those of polycrystalline wurtzite ZnO, matching JCPDS card No. 89-0510. The intensity of (100) and (101) peaks decreases with increasing Co doping in contrast to the (002)

peak which remains relatively unaltered with doping. With a smaller atomic structure factor for Co than Zn, originating with a smaller number of electrons, it may be expected that the diffracted peak intensities become smaller with increasing Co doping. The persistence of the (002) peak is taken to indicate a preferential *c*-axis growth direction for all samples.

The lattice parameters derived from XRD analysis are given in Table 1. In all cases the ratio of the unit cell axis lengths, *c/a*, is ~1.60 which is characteristic of the wurtzite ZnO structure. Further, the unit cell volume is denoted in Fig. 3. For the case of the doped samples, ZC1-4, the average unit cell volume of 46.72 $Å^3$ is ~4% less than that for undoped ZnO. Such a decrease is characteristic of substitution of the Zn^{2+} ion by the smaller radius Co^{2+} ion in tetrahedral configuration. [18] The slight increase in the unit cell volume for ZC3 and ZC4 relative to ZC1 and ZC2 may be indicative of Co^{2+} ions occupying interstitial sites in these more heavily doped samples.

The argument based on a *small* reduction in unit cell volume, combined with the lack of explicit observation of peaks corresponding to metallic cobalt or cobalt oxide phases gives support for the dominant substitutional inclusion of Co^{2+} on Zn^{2+} sites. In addition to the XRD data as presented in figure 3 we note that peaks for Co metal (~44.4°), Co_3O_4 (31.25°, 36.75°, 65.25°) or for CoO (42.5°, 62.25°) are not evident on a logarithmic scale or in terms of distorting the shape or increasing the full-width-half-maximum of the (100) and (101) diffraction peaks (very close to the 31.25° and 36.75° values for Co_3O_4) for ZnO when the diffractograms are examined on an expanded angle scale. However, the existence of very small Co nanoparticles cannot strictly be excluded by XRD data; while nanoparticles of ~5 nm diameter have yielded a distinct peak at ~44.4° in XRD [19], such particles of 3 nm diameter have been evidenced in atom probe tomography while leaving no signature in X-ray diffractograms [20]. It should be

6

remarked, though, that such metallic nanoparticles tend to be a feature of preparation by pulsed laser deposition [19, 20], rather than the crystallisation from solution method employed here. The final point of interest from the XRD data is that the Debye-Sherrer formula yields approximate grain sizes that are broadly in line with those obtained from the AFM images.

3.2.3 XPS

Core level XPS studies can reveal charge-transfer effects between Zn and Co, thus allowing determination of the oxidation state of Co in the host matrix. Fig. 4 depicts the core level spectra of (a) the whole scan range for all elements, (b) Zn2p, (c) Co2p and (d) O1s. The chemical states of the metallic elements present were analyzed by de-convoluting the spectra by means of fitting with Gaussian functions (not shown here). Starting with the Zn2p state the notable feature is its doublet nature, corresponding to Zn2$p_{3/2}$ and 2$p_{1/2}$ at ~1029 and ~1052 eV respectively. The spin orbit splitting is approximately constant for all samples at ~23.0 eV and the ratio of the areas under the peaks is close to a constant ratio of 3:2 as expected. However, there is some small variation in binding energy (BE), with the net consequence that the spin orbit splitting actually tends to increase slightly with Co content. A change in BE has been discussed in terms of electron transfer from the Zn4s level to the unfilled, high charge density Co3d level, which is an energetically favorable process [21-23]. Broadening of the Zn2$p_{3/2}$ and 2$p_{1/2}$ peaks for ZC1-4 relative to undoped ZnO – by ~350 meV on average for the Zn$p_{3/2}$ state and ~270 meV for Zn$p_{1/2}$ (see Table 1) - is indicative of either variation in the surface potential or the finite life time associated with a hole being filled by an electron from another shell.

A key point is the existence of shakeup satellites (denoted 'S' in Fig. 4) seen on the high-energy side of the core levels. In particular, this is significant for the case of the Co2p spectra since these constitute evidence for the existence of Co^{2+} ions. Comparison of the shapes and

7

positions of the primary and satellite peaks (Fig. 4c) shows that there is a good fit between the ZC1-4 films and the Co^{2+} standard [3, 5]. The spectra depict the characteristic peaks for $Co2p_{3/2}$ and $Co2p_{1/2}$ (Table 1), along with satellite peaks (~795 and ~812 eV) which are specifically connected with the +2 ionic state of Co [14, 24]. Taken together with the absence of XRD peaks corresponding to a Co-related phase this constitutes supporting evidence for Co in its oxidized (+2) state in the host lattice and substituted into the Zn^{2+} sites. Hence we conclude that Co exists in a high spin divalent state ($3d^7$, S=3/2), rather than metallic phase and is well incorporated into the ZnO lattice.

While the BE values for the Co dopant here are comparable to those of Co coordinated in an oxide lattice such as CoO, Co_2O_3 or Co_3O_4 [25], it is also noted that there is some small variation of the spectral line shapes and peak BE indicating that the local electronic structure of the Co impurities in ZnO depends (weakly) on doping concentration. The spin orbit splitting of $Co2p$ is close to literature values [14, 26], confirming the absence of metallic phase Co, but decreases slightly with doping (Table 1). The intensity of the $Co2p_{3/2}$ peak for ZC1 with respect to the satellite peak is low due to the small amount of Co embedded into ZnO lattice [23]. As the Co wt% increases the intensity of the main $2p_{3/2}$ peak relative to the satellite increases, while the ratio of the areas under the main peaks ($2p_{3/2}$, $2p_{1/2}$) remains approximately constant. Asymmetric peak structure is observed in the O1s spectra for all the films (see Table 1). For ZnO the asymmetric peak is resolvable in to three components lying at 539.5, 540.8 and 541.0eV (see Table 1). The main peak at 539.5 eV can be attributed to oxygen incorporated in the ZnO lattice, whereas the two shoulders may be attributed to chemisorbed oxygen [27]. However, the O1s peaks for ZC1-4 can all be fitted well with only two Gaussian curves, peaked at (averaged)

values of 538.9 and ~540.8 eV (Table 1) where the latter is the more intense, indicating a greater presence of chemisorbed oxygen.

3.3 Optical characterisation and defect analysis

3.3.1 Optical absorption

The transparent nature of ZnO is a distinctive and critically important feature of this semiconducting material as outlined in the introduction, so it is important to confirm that it is not compromised with Co doping. Fig. 5, which shows room-temperature UV-visible absorption spectra of Co-doped ZnO films along with that for pristine ZnO, indeed offers such confirmation.

Moving from the visible to the UV region (350-400 nm), the onset of heavy absorption is associated with the interband transition in the material. Unusually, though not uniquely, for the case of the undoped ZnO the main absorption edge exhibits some structure [28, 29]. However, the important point to note is that, for all samples, the onset of significant absorption remains below ~400 nm wavelength ensuring excellent transparency (average of <0.1 absorbance) across the visible range.

Assuming a direct interband transition, a plot of $(-\ln T \times h\nu)^2$ against $h\nu$, (T-transmission, h-Planck's constant, ν-frequency in Hz ; graphs not shown here) yields values for the band gap, E_g, as quoted in Table 1. These increase from 3.30 eV for undoped ZnO to ~3.43 eV for ZC1 and appear to saturate at ~3.47/8 eV for ZC2-ZC4. This increase in band gap with increasing Co doping is in contrast to the decrease found in Co-doped ZnO films prepared by sol-gel [16] and hydrothermal [30] techniques, although in both cases the doping extended to higher levels than in this study. By contrast, but in common with the data presented here, an increase of band gap has been reported with increased concentration for the cases of Co [19, 31] and Ga [32] dopants. This blue-shift phenomenon may be understood in terms of the Burstein-Moss effect [33]. Also,

alluding forward to the PL data of section 3.3.2 it is interesting to note that, in the work by Makino et al. [32], the shift of band gap to higher energies is not tracked by the centre-wavelength of the PL, a feature which we also find here and in our previous work on similarly prepared nanowires [29].

The optical absorption spectrum of Fig. 5 shows a minor feature at ~500 nm which may be instrumental in origin, but displays no evidence of absorption peaks at 570, 615 and 655 nm characteristic of ionic Co, such as observed by Ivill et al.[19], Bouloudenine et al. [30] and H Ndilimabaka et al. [34]. That these peaks (which are of the order of 0.01 on the absorbance scale) are not observed in our data is not surprising since the samples we report on have at least an order of magnitude less Co content than those in the cited works on account of their relatively low Co concentration and small thickness.

3.3.2 Photoluminescence

The PL response of the undoped and Co-doped ZnO films is shown in Figure 6 where the inset depicts a magnified view from 3.35-3.05 eV. Although samples of all doping levels show an exciton band with the peak of the emission at values in the range 3.22 to 3.26 eV, consistent with values in the literature [35], it is noticeable that PL due to this transition becomes heavily attenuated with increasing Co doping. We consider that this effect is connected with the greater level of chemisorbed oxygen on the cobalt-doped samples, as indicated from the XPS data relating to the O1s peak (Fig. 4d). Chemisorbed oxygen takes ups or effectively traps electrons from the ZnO, leading to a depletion layer in the semiconductor material. These electrons are thus no longer available for exciton formation and subsequently for electron-hole recombination and this in turn leads to a decrease in PL of excitonic origin. The role of chemisorbed oxygen has

been well studied in the context of ZnO-based devices [36] where its presence has been noted as reducing exciton emission; however, the main issue in that context comprises the long time constants involved in device photoresponse due to charge trapping in the chemisorption process.

Considering next the visible spectral range, we note that while it has been reported that PL decreases with increasing Co doping [37] significant PL persists in Co-doped ZnO samples of various types [14, 23, 29, 38]. Starting at the short-wavelength end of the visible, a violet band, centered at 2.96 eV, due to zinc interstitials (Zn_i) appears in the case of the ZnO film. Like the main exciton band at 3.23 eV, this band is suppressed, though less significantly, upon doping (cases ZC2-ZC4) - the intensity ratio, $PL_{3.24}/PL_{2.98}$, is given in Table 1 for all samples – where the violet peak shifts to marginally higher energy (2.98 eV). This feature can be attributed to band edge exciton transitions [23, 39], specifically from the strong *sp-d* exchange interactions between the band electrons and the localized electrons of the Co [14, 23]. The PL evident in the region of 2.85 eV, in only the case of ZC1, is due to transitions from Zn_i to Zn vacancy (V_{Zn}).

Continuing towards lower energies it is generally accepted that the PL centered at ~2.35 eV is due to oxygen vacancies (V_O). While this is weak in the case of the pure ZnO sample, it is clear that a more significant level of V_O has been introduced in the doping process, as evidenced by the strong PL centred at 2.34 eV in the case of all the doped samples. This PL is due to the transition of photogenerated electrons from a deep level below the conduction band (associated with the V_O) to a deeply trapped hole [23, 40]. On the matter of the imperfect incorporation of oxygen in the lattice a very weak band at 1.98 eV, due to oxygen interstitials (O_i), can be noticed for the case of ZnO. The intensity of this PL band decreases for the case of ZC1 and disappears for higher dopings. This removal of O_i from the material appears to be a consistent concomitant of the increased density of V_O's.

The intensities of visible bands of PL are often referenced to that in the UV (due to exciton emission) as a measure of crystal defect density and this has been carried through in Table 1 for comparative purposes. However, in the case of the samples studied here such a ratio – or rather its inverse - is a measure of internal lattice defects relative to the occurrence of chemisorbed oxygen, rather than any meaningful measure of 'crystallinity'. In any case it is clear that for ZC1-4 there is significant emission in the green-red regime (wavelength 475 – 600 nm or energy 2.6 - 2.1eV), a feature that has important bearing on the wavelength selective photoresponse of ZnO-based detectors [41-44].

3.3.3 Raman Spectroscopy

Raman spectroscopy is a versatile technique for detecting dopant incorporation and the resulting defects and lattice disorder in a host lattice, especially in relation to the detection of material segregations or secondary phases in the dopant system. Fig. 7 shows composition-dependent room temperature Raman spectra of the films with the various modes and their designations annotated. The most prominent peaks are those at 241 cm^{-1} and 439 cm^{-1} E_2 (high), where there is some quite remarkable contrast between the samples. The latter branch is characteristic of a wurtzite crystal structure [18] of high crystalline integrity. This band is suppressed in samples ZC1 and ZC2, indicating reduced crystallanity [1], while the more heavily doped samples, ZC3 and ZC4, show significant retrieval of the intensity level of pristine ZnO. The suppression of the 439 cm^{-1} peak is likely due to the presence of strain in the material. Hays et al. [37] observed a progressive attenuation of the E_2 mode with increasing Co concentration in ZnO which they attributed to increased strain induced by an increase in the density of Co occupying interstitial sites. Here, however, with the less heavily doped samples (ZC1 and ZC2) displaying attenuation of the 439 cm^{-1} peak, we suggest that in these cases the origin of the strain

is at the interface between the substrate and the thin samples. Arguably this is also manifest in the less well developed grain structure of samples ZC1 and ZC2 compared to samples ZC3 and ZC4 (Fig. 1 and 2).

The band at 241 cm^{-1} is not readily identified, but we note that there is a peak in the calculated phonon density of states for ZnO at this wavenumber [45] although it appears that this is not normally observed. Indeed, there is no occurrence of a Raman peak at precisely this wavenumber in an extensive catalogue of (transition and other) metal compounds [46] but it is interesting to note that a strong peak has been observed at 240 cm^{-1} in nanophase TiO$_2$ [47] which was not clearly identified but was attributed to a long range order effect, occurring when bands known to be characteristic of the crystal structure were strong. This is the case here, where for samples ZC3 and ZC4, the 241 cm^{-1} band displays virtually full recovery of the ZnO level, while ZC1 and ZC2 show almost no discernible feature at this wavenumber. In summary, the better quality crystalline behavior of samples ZC3 and ZC4 that is evident in the SAED patterns is manifestly emphasised in the Raman spectra. The next most prominent feature is centered at 547 cm^{-1}, which is attributed to donor defects such as V_O's or Zn_i's [18, 48] and, consistent with the evidence of PL where green (~2.35 eV) emission indicates V_O's, is least developed for the case of undoped ZnO. These defects, which are bound to tetrahedral Co sites, give rise to a quasi-longitudinal optical phonon mode and are pertinent to the discussion on magnetic properties (section 3.3.3.1)

In addition, other modes such as 2E$_2$ (low) (330 cm^{-1}) and A$_1$ (TO) (370 cm^{-1}) are observed. The broad peak centered at ~330 cm^{-1} corresponds to the second order phonon mode of 2E$_2$ (low) due to zone boundaries [49]. A very weak feature at 472 cm^{-1} due to surface phonon modes [1] is also present. The disappearance of some of the phonon modes of ZnO, e.g. that at

330 cm^{-1}, for low Co doping levels reflects the distortion of the local atomic arrangement around the magnetic impurities. Nevertheless, in XRD it was possible to still observe wurtzite structure for all doping levels. Finally, it is notable that there are no peaks corresponding to Co oxides indicating segregation-free ZnO. Also, there are no Co-induced shifts in the main Raman peaks which is evidence that the doping has not given rise to significant strain on the host lattice.

3.3.3.1 Comment on magnetic properties with reference to Raman data

For this part of the investigation samples ZC3 and ZC4 were selected because of their higher Co-doping density and better crystalline quality as evidenced on the basis of electron diffraction and Raman results. They were tested in a magnetic field of field strength in the range $\pm 10^4$ Oe that was available to us, but the response appears to be essentially paramagnetic in nature. We consider this aspect of the study with reference to the work of Singhal et al. [50] in which it was noted that a ferromagnetic response did not develop in Co-doped ZnO nanocrystals until the Co doping reached higher levels – namely, samples with 5 or 7 wt% of Co in that case. They interpreted their results in the framework of a bound magnetic polaron mechanism proposed by Coey et al. [51, 52]. This requires a high density of donor defects, specifically V_O and Zn_i in the present context, which overlap to form a donor impurity band that interacts with local magnetic moments through the formation of bound magnetic polarons. When both the magnetic impurities are of sufficient density and the bound, finite-radius polaron states overlap to form a continuous chain in the material, then ferromagnetism is mediated. It is interesting to note that only when the Raman band at 546 cm^{-1} (547 cm^{-1} in our spectra), i.e. the signature of V_O's and Zn_i's, is of greater intensity than that at 437 cm^{-1} (439 cm^{-1} in our spectra) that ferromagnetism is observed [50]. When the opposite is true, as is the case for samples ZC1-4 here, then ferromagnetism is not present. Thus, while ferromagnetic behavior is not observed in

the samples of this study, its absence may be rationalised with reference to the recorded Raman spectra and the bound magnetic polaron model developed by Coey et al. [51, 52]; equally, the potential to develop such desired behavior at slightly higher Co doping is promising.

4. Summary and conclusions

A simple solution-based growth technique has been reported for the fabrication of thin, Co-doped (1-4 wt%) ZnO and undoped ZnO films. Generally good quality wurtzite structure was confirmed by XRD, while SAED showed high single-crystal integrity on a local scale from samples ZC3 and ZC4 which, according to AFM imaging, had large (>100 nm) grain structure; the smaller-grained samples, ZC1 and ZC2, yielded typical polycrystalline diffraction ring SAED patterns. Also, for ZC3 and ZC4, TEM images illustrated well-oriented lattice planes of interplanar spacing 0.26 nm, characteristic of (002) planes, while the (002) peak in the XRD scans remains the most prominent peak as the Co-doping increases. The smaller unit cell volume for the doped samples, extracted from XRD data, is indicative of Co^{2+} substitution of Zn^{2+} in the lattice while XPS analysis gave evidence of Co in a high-spin, +2 oxidation state. There is no evidence of the segregation of cobalt metal or cobalt oxide phases within the limits of detection of Raman spectroscopy and XRD analysis.

A crucial aspect of the study is the defect analysis where PL spectra show clear evidence of V_O in the doped samples, Zn_i and some O_i in the case of undoped ZnO. Despite such defects the material retains very good transparency across the doping range with a bandgap that increases from 3.30 eV for undoped ZnO to close to 3.50 eV for the more heavily Co-doped samples. Also, it appears that the greater levels of chemisorbed oxygen that are inferred from the XPS data for the O1s peak for doped samples ZC2-ZC4 (and to a lesser extent ZC1) act to

15

quench the ultraviolet (exciton) PL due to electron trapping. The lack of ferromagnetic behavior is attributed to an insufficient density of impurity states (as evidenced in the Raman spectra) and of magnetic impurities in the framework of a bound magnetic polaron picture.

To conclude, undoped and doped ZnO polycrystalline, thin films have been fabricated on quartz substrates using sequential spin-casting and annealing of simple salt solutions. The Co is well incorporated in the lattice i.e. is tetrahedrally coordinated on the Zn sites and of charge +2 in a high spin electronic state, without altering the wurzite structure and there is no detectable evidence of the precipitation of cobalt oxide phases within the scope of the characterisation techniques employed here. The samples retain high transparency with increasing doping but do not develop a ferromagnetic response.

Acknowledgements

References

[1]   H.J. Zhou, L.M. Chen, V. Malik, C. Knies, D.M. Hofmann, K.P. Bhatti, S. Chaudhary, P.J. Klar, W. Heimbrodt, C. Klingshirn, H. Kalt, Phys. Status Solidi A 204/1 (2007) 112.
[2]   M. Schumm, M. Koerdel, S. Muller, C. Ronning, E. Dynowska, Z. Golacki, W. Szuszkiewicz, J. Geurts, J. Appl. Phys. 105/8 (2009).
[3]   A.C. Tuan, J.D. Bryan, A.B. Pakhomov, V. Whutthanandan, S. Thevuthasan, D.E. McCready, D. Gaspar, M.H. Engelhard, J.W.R. Jr., K. Krishnan, D.R. Gamelin, S.A.Chambers, Phys. Rev. B 70 (2004) 054424.
[4]   H.J.Lee, S. Jeong, C. Cho, CH.Park, Appl. Phys. Lett. 81 (2002) 4020.
[5]   X.J. Liu, C. Song, F. Zeng, F. Pan, Thin Solid Films 516 (2008) 8757.

[6]   J. K.Furdyna, J. Kossut, Diluted Magnetic Semiconductors (Semiconductors and Semimetals), Academic, New York, 1988.

[7]   S.A. Wolf, D.D. Awschalom, R.A. Buhrman, J.M. Daughton, S. von Molna´r, M.L. Roukes, A.Y. Chtchelkanova, D.M. Treger, Science 294 (2001) 1488.

[8]   H. Ohno, F. Matsukura, Y. Ohno, JSAP Int. 5 (2002) 4.

[9]   K. Ando, S. Sugano, N. Kojima, In Solid-State Sciences: Magneto-Optics, Springer, New York, 2000.

[10]   S.J. Pearton, C.R. Abernathy, M.E. Overberg, G.T. Thaler, D.P. Norton, N. Theodoropoulou, A.F. Hebard, Y.D. Park, F. Ren, J. Kim, L.A. Boatner, J. Appl. Phys 93 (2003) 1.

[11]   X.T. Wang, L.P. Zhu, Z.G. Ye, Z.Z. Ye, B.H. Zhao, J. Inorg. Mater. 25/7 (2010) 711.

[12]   M. Millot, J. Gonzalez, I. Molina, B. Salas, Z. Golacki, J.M. Broto, H. Rakoto, M. Goiran, J. Alloy. Compd. 423/1-2 (2006) 224.

[13]   A. El Manouni, M. Tortosa, F.J. Manjon, M. Mollar, B. Mari, J.F. Sanchez-Royo, Microelectr. J. 40/2 (2009) 268.

[14]   S. Wang, P. Li, H. Liu, J.B.A. Li, Y. Wei, J. Alloy.Compd. 505/1 (2010) 362.

[15]   Y. Wang, L. Sun, L.G. Kong, J.F. Kang, X. Zhang, R.Q. Han, J. Alloy. Compd. 423/1-2 (2006) 256.

[16]   L. Wei, Z.H. Li, W.F. Zhang, Appl. Surf. Sci. 255/9 (2009) 4992.

[17]   V. Djara, J.C.Bernede, Thin Solid Films 493 (2005) 273.

[18]   D.W. Chu, Y.P. Zeng, D.L. Jiang, J. Phys. Chem. C 111/16 (2007) 5893.

[19]   M. Ivill, S.J. Pearton, S. Rawal, L. Leu, P. Sadik, R. Das, A.F. Hebard, M. Chisholm, J.D. Budai, D.P. Norton, New J. Phys. 10 (2008) 065002.

[20]   R. Lardé, E. Talbot, P. Pareige, H. Bieber, G. Schmerber, S. Colis, V. Pierron-Bohnes, A. Diana, J. Am. Chem. Soc. 133 (2011) 1451.

[21]   X. Wang, J. Xu, B. Zhang, H. Yu, J. Wang, X. Zhang, J. Yu, Q. Li, Adv. Mater. 18 (2006) 2476.

[22]   K.R.Kittilstved, Nat. Mater. 5 (2006) 291.

[23]   S. Bhattacharyya, A. Gedanken, J. Phys. Chem. C 112/12 (2008) 4517.

[24]   B.Q. Wang, C.H. Xia, J. Iqbal, N.J. Tang, Z.R. Sun, Y. Lv, L.N. Wu, Solid State Sci. 11 (2009) 1419.

[25]   B.J. Tan, K.J. Klabunde, P.M.A. Sherwood, J. Am. Chem. Soc. 113 (1991) 855.

[26]   J. F. Moulder, W. F. Stickle, P. E. Sobol, K.D. Bomben, Handbook of X-ray Photoelectron Spectroscopy, Perkin-Elmer, Eden Prairie, MN, 1992.

[27]   S. Hullavarad, N. Hullavarad, D. Look, B. Claflin, Nanoscale Res. Lett. 4/12 (2009) 1421.

[28]   S.T. Tan, B.J. Chen, X.W. Sun, X. Hu, X.H. Zhang, S.J. Chua, J. Cryst. Growth 281 (2005) 571.

[29]   S. Vempati, A. Shetty, P. Dawson, K. Nanda, S.B. Krupanidhi, J. Cryst. Growth 343 (2012) 7.

[30]   M. Bouloudenine, N. Viart, S. Colis, A. Dinia, Catal. Today 113 (2006) 240.

[31]   X.J. Liu, C. Song, F. Zeng, F. Pan, Thin Solid Films 516 (2008) 8757.

[32]   T. Makino, Y. Segawa, S. Yoshida, A. Tsukazaki, A. Ohtomo, M. Kawasaki, Appl. Phy. Lett. 85 (2004) 759.

[33]   E. Burstein, Phys. Rev. B 93 (1953) 632.

[34]   H. Ndilimabaka, S. Colis, G. Schmerber, D. Müller, J.J. Grob, L. Gravier, C. Jan, E. Beaurepaire, A. Dinia, Chem. Phys. Lett. 421 (2006) 184.

[35]   C.L. Dong, C. Persson, L. Vayssieres, A. Augustsson, T. Schmitt, M. Mattesini, R. Ahuja, C.L. Chang, J.-H. Guo, Phys. Rev. B 70 (2004) 195325.

[36]   Z.-M. Liao, H.-Z. Zhang, D.-P. Yu, Appl. Phy. Lett. 97 (2010) 033113.

[37]   J. Hays, K.M. Reddy, N.Y. Graces, M.H. Engelhard, V. Shutthanandan, M. Luo, C. Xu, N.C. Giles, C. Wang, S. Thevuthasan, A. Punnoose, J. Phys.: Condens. Mater 19 (2007) 266203.

[38]   R. Maity, S. Das, M.K. Mitra, K.K. Chattopadhyay, Physica E 25 (2005) 605.

[39]   Q. Tang, W. Zhou, J. Shen, W. Zhang, L. Kong, Y. Qian, Chem. Comm. (2004) 712.

[40]   C.G. Kim, K. Sung, T.M. Chung, D.Y. Jung, Y. Kim, Chem. Comm. (2003) 2068.

[41]   K. Keem, H. Kim, G.-T. Kim, J.S. Lee, B. Min, K. Cho, M.-Y. Sung, S. Kim, Appl. Phy. Lett. 84/22 (2004) 4376.

[42]   Z. Fan, P.-c. Chang, J.G. Lu, E.C. Walter, R.M. Penner, C.-h. Lin, H.P. Lee, Appl. Phy. Lett. 85/25 (2004) 6128.

[43]   Y. Liu, Z. Zhang, H. Xu, L. Zhang, Z. Wang, W. Li, L. Ding, Y. Hu, M. Gao, Q. Li, L.-M. Peng, J. Phys. Chem. C 113 (2009) 16796.

[44]   S. Vempati, S. Chirakkara, J. Mitra, P. Dawson, K.K. Nanda, S.B. Krupanidhi, Appl. Phy. Lett. 100 (2012) 162104.

[45]   A. Kaschner, U. Haboeck, M. Strassburg, M. Strassburg, G. Kaczmarczyk, A. Hoffmann, C. Thomsen, A. Zeuner, H.R. Alves, D.M. Hofmann, B.K. Meyer, Appl. Phys. Lett. 80 (2002) 1909.

[46]   M. Bouchard, D.C. Smith, Spectrochim. Acta A 59/10 (2003) 2247.

[47]   C.A. Melendres, A. Narayanasamy, V.A. Maroni, R.W. Siegel, J. Mater. Res. 4/5 (1989) 1246.

[48]   C.L. Du, Z.B. Gu, M.H.Lu, J. Wang, S.T. Zhang, J. Zhao, G.X. Cheng, H. Heng, Y.F.Chen, J. Appl. Phys. 99 (2006) 123515.

[49]   J.M. Callejy, M. Cardona, Phys. Rev. B 16 (1977) 3753.

[50]   A. Singhal, S.N. Achary, J. Manjanna, S. Chatterjee, P. Ayyub, A.K. Tyagi, J. Phys. Chem. C 114/8 (2010) 3422.

[51]   J.M.D. Coey, M. Venkatesan, C.B. Fitzgerald, Nat. Mater 4 (2005) 173.

[52]   J.M.D. Coey, J. Appl. Phys. 97 (2005) 10D313.

Figure Captions

Figure 1. Tapping mode AFM images of Co-doped ZnO films. ZC1-4 denote Co-doped ZnO samples with 1 to 4 wt% Co respectively.

Figure 2. HRTEM images (left) of samples ZC1 and ZC3 (Co-doped ZnO with 1 and 3 wt% Co respectively), and corresponding SAED patterns (right).

Figure 3. XRD patterns of ZnO and Co-doped ZnO samples. ZC1-4 denote Co-doped ZnO samples with 1 to 4 wt% Co respectively.

Figure 4. XPS spectra for Co-doped ZnO (a) whole scan range, (b) Zn2p, (c) Co2p, (d) O1s. Satellite peaks are denoted by 'S'. ZC1-4 denote Co-doped ZnO samples with 1 to 4 wt% Co respectively.

Figure 5 Room-temperature UV-visible absorption spectra for ZnO and Co-doped ZnO samples. ZC1-4 denote Co-doped ZnO samples with 1 to 4 wt% Co respectively.

Figure 6 Photoluminescence spectra from ZnO and ZC1-4 under excitation of laser input at 355 nm. ZC1-4 denote samples with 1, 2, 3 and 4 wt% Co respectively.

Figure 7. Raman spectra of Co-doped ZnO thinfilms compared with ZnO; excitation was by laser operating at wavelength 532 nm. ZC1-4 denote samples with 1, 2, 3 and 4 wt% Co respectively.

Table 1. Consolidated data values for undoped ZnO and for the various cobalt-doped ZnO samples, ZC1-4, where the number indicates the wt% doping of Co. BE = Binding energy; PL refers to the intensity of a photoluminescence peak where the numerical subscript is the peak position in eV.
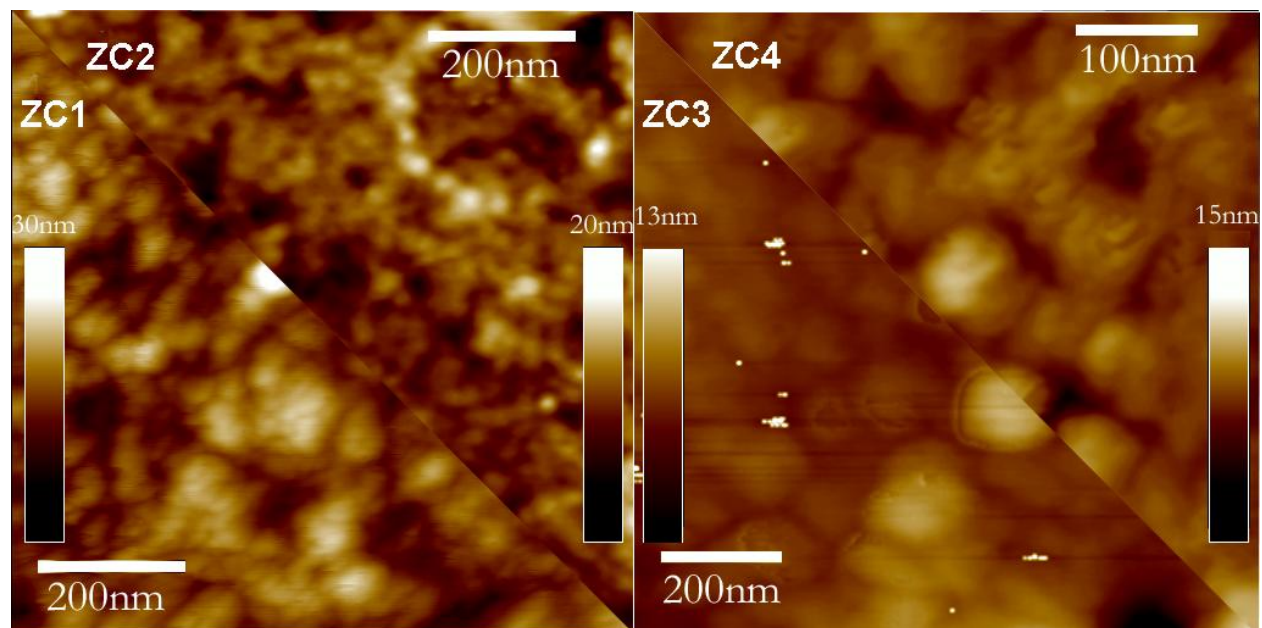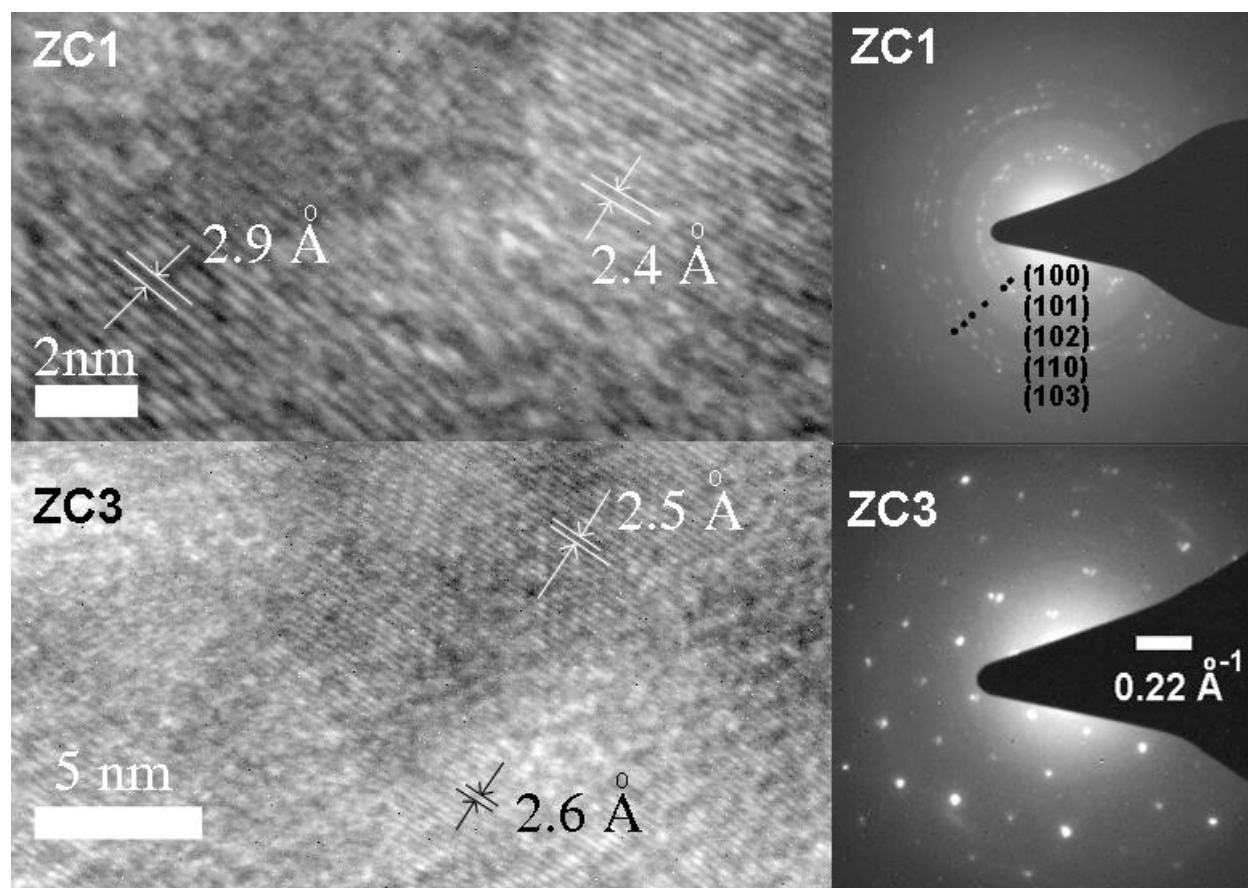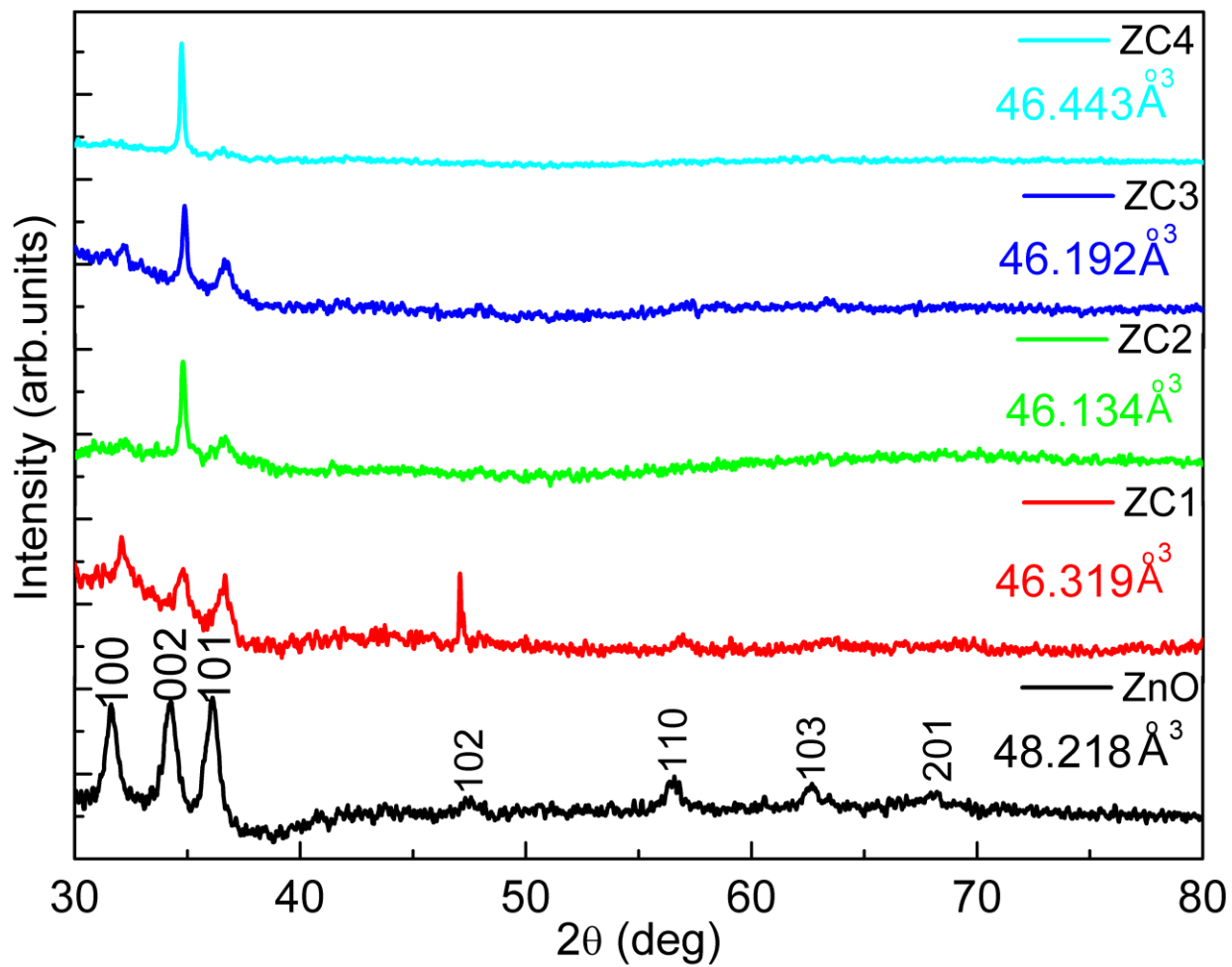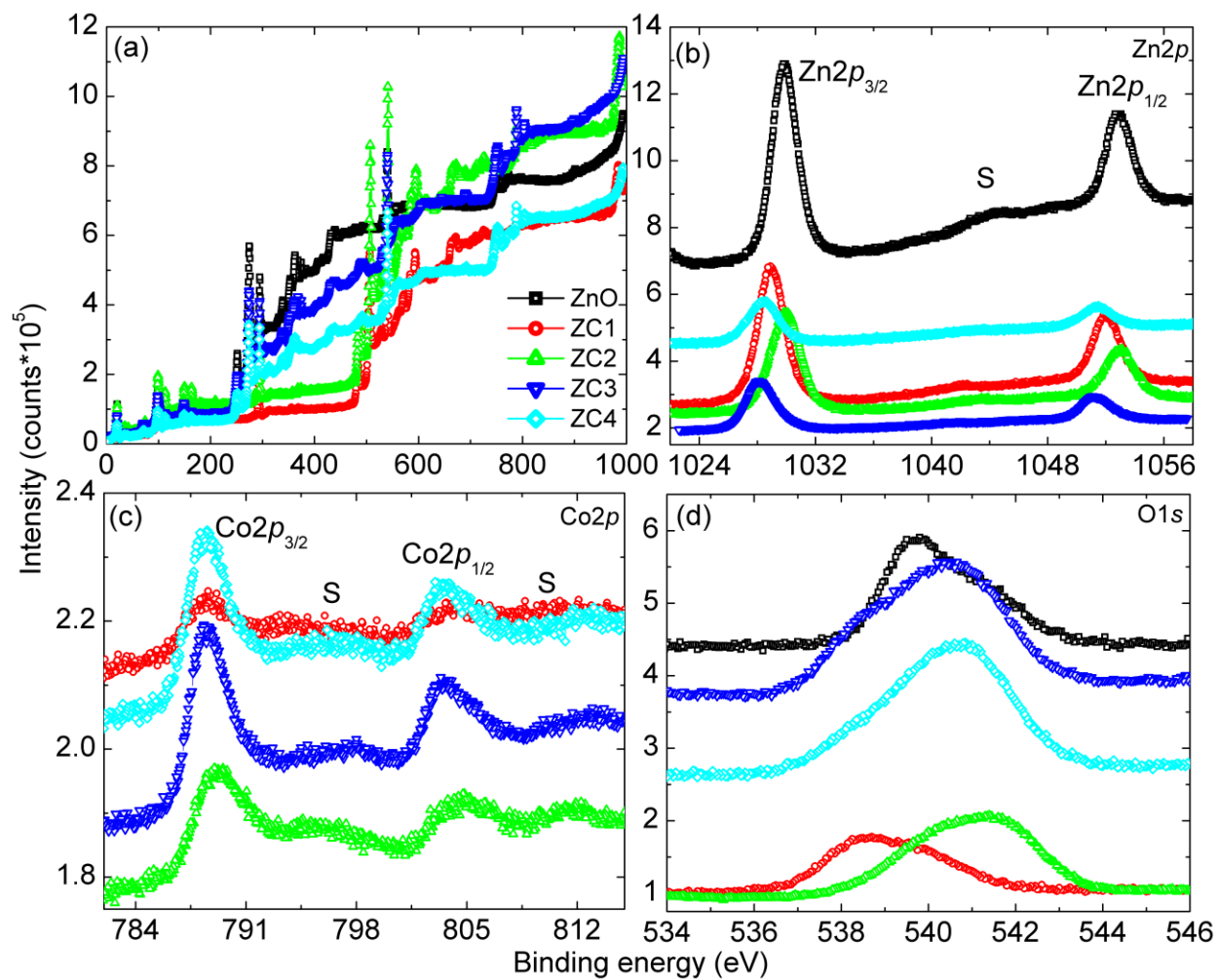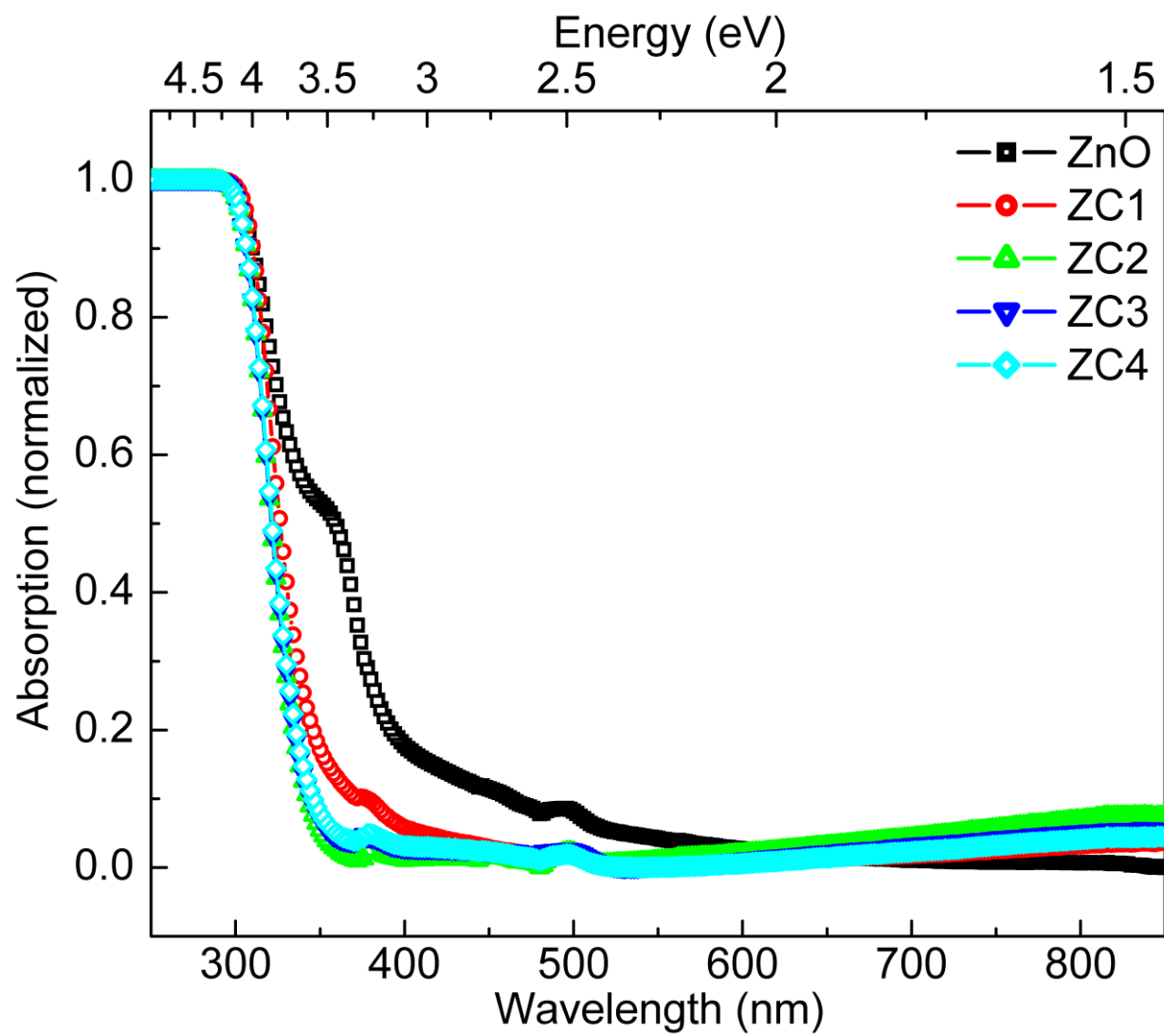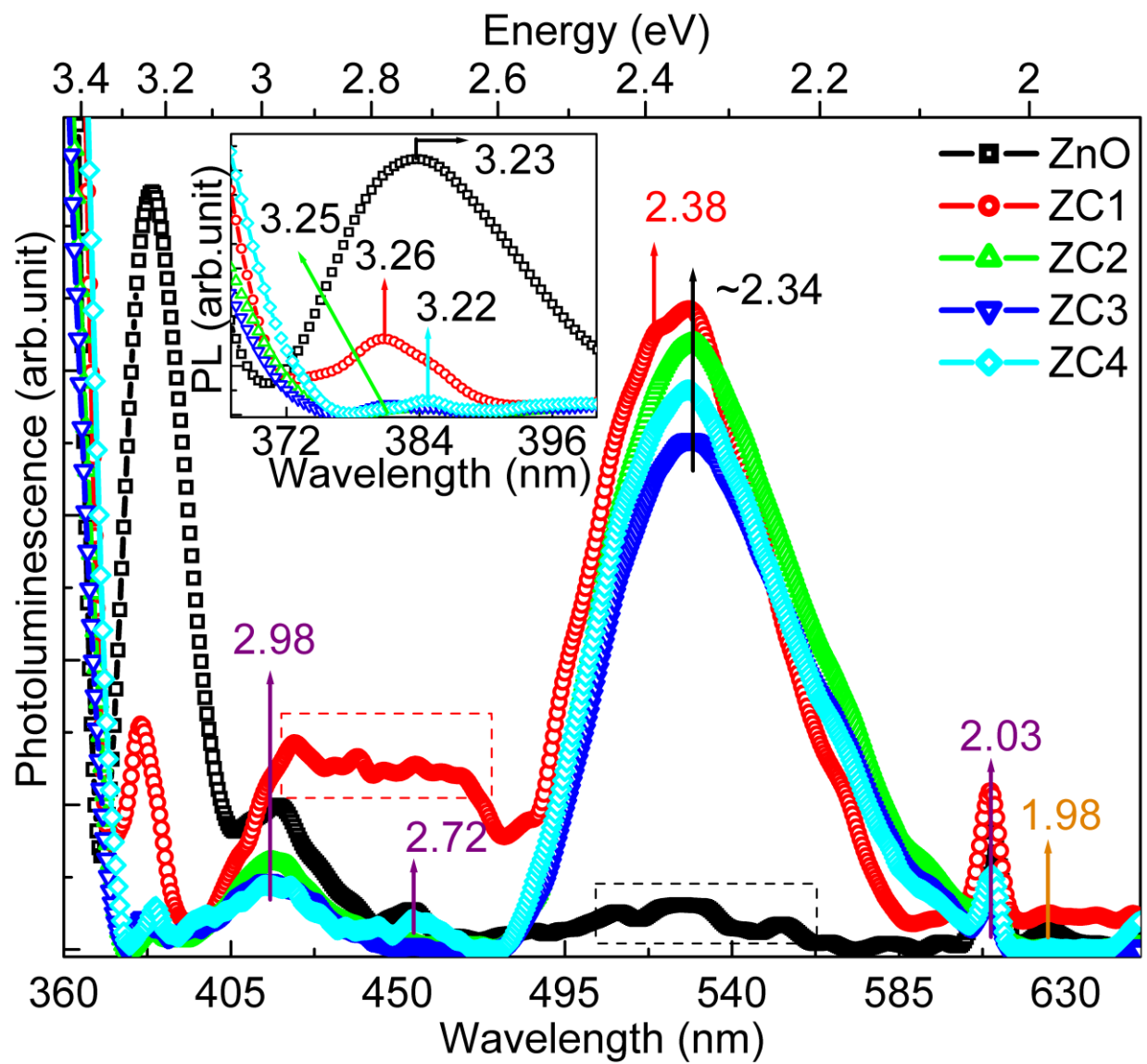
Fig. 1

Fig. 2

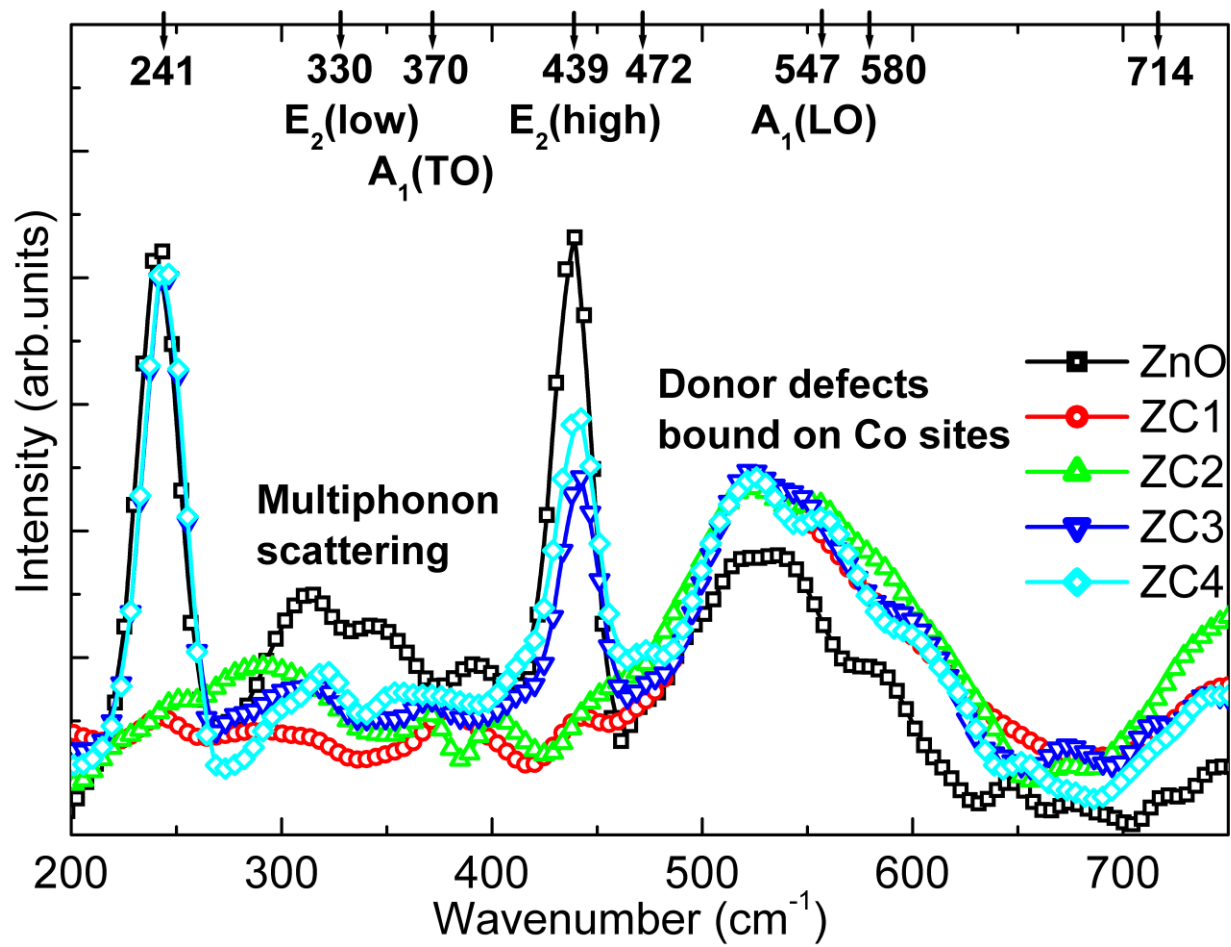Fig. 3

Fig. 4

Fig. 5

Fig. 6

Fig. 7

Table 1. Consolidated data values for undoped ZnO and for the various cobalt-doped ZnO samples, ZC1-4, where the number indicates the wt% doping of Co. BE = Binding energy; PL refers to the intensity of a photoluminescence peak where the numerical subscript is the peak position in eV.

Technique and Parameters measured		Sample				
		ZnO	ZC1	ZC2	ZC3	ZC4
XRD	a (Å)	3.263	3.227	3.212	3.220	3.222
	c (Å)	5.229	5.135	5.162	5.146	5.165
XPS	All units in eV					
	FWHM for Zn2$p_{3/2}$	1.80	2.01	2.30	2.10	2.20
	FWHM for Zn2$p_{1/2}$	2.04	2.12	2.40	2.21	2.51
	Shift in BE w.r.t. ZnO	-	0.90	0.025	1.66	1.50
	Peak energy, Co2$p_{3/2}$	-	789.01	789.63	788.69	788.59
	Peak energy Co2$p_{1/2}$	-	805.28	804.87	803.91	803.71
	Spin orbit splitting		16.27	15.24	15.22	15.13
	O1s - lattice	539.5	538.2	539.8	538.5	539.1
	O1s - chemisorbed	540.8	541.0	541.4	540.6	540.9
		541.0				
Optical absorption	λ_0 (nm)	365.2	356.1	374.7	371.2	376.0
	$h\nu_{onset}$ (eV)	3.395	3.482	3.309	3.341	3.298
	E_g (eV)	3.5	3.48	3.52	3.52	3.53
	FWHM (nm)	14	9	6	4	3
Photo-luminesence Intensity ratio	PL$_{3.24}$/PL$_{2.98}$	5.3	1.2	0.2	0.5	0.6
	PL$_{3.24}$/PL$_{2.35}$	16.7	0.4	0.03	0.06	0.07
	PL$_{3.24}$/PL$_{2.03}$	6.25	1.4	0.4	0.7	0.6

Highlights

- Simple solution-based method for the fabrication of Co-doped ZnO thin films.
- Evidence for Co substitution on Zn sites in +2 oxidation state.
- ZnO, with up to 4% Co doping, retains high transparency across visible spectrum.
- Quenching of exciton photoluminescence linked to chemisorbed oxygen in Co-doped ZnO